Inter-Kramers Transitions and Spin-Phonon Couplings in a Lanthanide-Based Single-Molecule Magnet

Duncan H. Moseley,[a] Shelby E. Stavretis,[a] Zhenhua Zhu,[b] Mei Guo,[b] Craig M. Brown,[c] Mykhaylo Ozerov,[d] Yongqiang Cheng,[e] Luke L. Daemen,[e] Rachael Richardson,[f] Gary Knight,[f] Komalavalli Thirunavukkuarasu,[f] Anibal J. Ramirez-Cuesta,[e] Jinkui Tang,[b] Zi-Ling Xue[a,]*

[a] *Department of Chemistry, University of Tennessee, Knoxville, Tennessee 37996, United States*

[b] *State Key Laboratory of Rare Earth Resource Utilization, Changchun Institute of Applied Chemistry, Chinese Academy of Sciences, Changchun 130022, P. R. China*

[c] *Center for Neutron Research, National Institute of Standards and Technology, Gaithersburg, Maryland 20899, United States*

[d] *National High Magnetic Field Laboratory, Tallahassee, Florida 32310, United States*

[e] *Neutron Scattering Division, Oak Ridge National Laboratory, Oak Ridge, Tennessee 37831, United States*

[f] *Department of Physics, Florida A&M University, Tallahassee, Florida 32307, United States*

Abstract. Spin–phonon coupling plays a critical role in magnetic relaxation in single-molecule magnets (SMMs) and molecular qubits. Yet, few studies of its nature have been conducted. Phonons here refer to both intermolecular and intramolecular vibrations. In the current work, we show spin–phonon couplings between IR-active phonons in a lanthanide molecular complex and Kramers doublets (from the crystal field). For the SMM $Er[N(SiMe_3)_2]_3$ (**1**, Me = methyl), the couplings are observed in far-IR magnetospectroscopy (FIRMS) of crystals with coupling constants ≈ 2-3 cm^{-1}. In particular, one of the magnetic excitations couples to at least two phonon excitations. FIRMS reveals at least three magnetic excitations (within the $^4I_{15/2}$ ground state/manifold; hereafter manifold) at 0 T at 104 cm^{-1}, ~180 cm^{-1}, and 245 cm^{-1}, corresponding to transitions from ground state, $M_J = \pm 15/2$, to the first three excited states, $M_J = \pm 13/2$, ±11/2, and ±9/2, respectively. The transition between the ground and first excited Kramers doublet in **1** is also observed in inelastic neutron scattering (INS) spectroscopy, moving to higher energy with increasing magnetic field. INS also gives complete phonon spectra of **1**. Periodic DFT computations provide the energies of all phonon excitations, which compare well with the spectra from INS, supporting the assignment of the inter-Kramers-doublet or magnetic transition in the spectra. The current studies unveil and measure the spin–phonon couplings in a typical lanthanide complex and throw light on the origin of the spin–phonon entanglement.

Introduction

The discovery in the early 1990s that the molecular cluster compound $Mn_{12}O_{12}(OAc)_{16}(H_2O)_4$ ($Mn_{12}Ac$; OAc = acetate) could retain its magnetization for long periods of time in the absence of an external magnetic field[1-2] led to great excitement and intense research in a class of magnetic materials known as single-molecule magnets (SMMs).[3] The strong interests in SMMs stem from their intrinsic properties as molecular analogues of classical bulk ferromagnets and potential applications in, for example, data storage and processing. In 2003, slow magnetic relaxation was reported in mononuclear rare-earth complexes,[4] followed by observation of similar SMM behaviors in a mononuclear transition metal compound around 2010. These mononuclear compounds of both lanthanides and transition metals form a sub-class of SMMs known as single-ion magnets (SIMs).[5-16] Due to their inherent large first-order spin-orbit coupling, lanthanide complexes are described by their total angular momentum states (M_J) as opposed to many transition metal complexes, which are often described by their spin (M_S)

states.[7] Interactions between the electron density of the lanthanide ion and the crystal-field environment lead to anisotropies required for effective single-ion magnets, as Rinehart and Long laid out clearly.[5] As a result of the *f* orbital participation through first-order spin-orbit coupling, the magnetic anisotropy barriers separating opposite orientations of the spin ground states in lanthanide SIMs tend to be higher than the transition metal SIMs which often rely on electronic spin as the only significant source of angular momentum in the compounds. These properties have attracted great interest and extensive work in finding lanthanide SIMs with unique ligands, giving large spin reversal barriers.[4-11, 17-26]

There are two requirements for a lanthanide compound to be an effective SIM:[5] (1) The ground state should be doubly-degenerate with a high magnitude quantum number M_J. This is because the bistability ($\pm M_J$) of its ground state is a critical feature of a SIM. In the absence of a magnetic field, breaking the $\pm M_J$ degeneracy is forbidden for a Kramers ion (with an odd electron count). (2) There must be a large separation between the ground and the first excited states. For the f^{11} Er^{3+} ion [$L = 6$, $S = 3/2$, ground-state (or ground-manifold) term symbol $^4I_{15/2}$], Hund's second rule (maximizing orbital angular multiplicity) leads to the ground-state electronic configuration of $4f_{x(x^2\text{-}3y^2)}{}^2 4f_{z(x^2\text{-}y^2)}{}^2 4f_{xz^2}{}^2 4f_{z^3}{}^2 4f_{yz^2}{}^1 4f_{xyz}{}^1 4f_{y(3x^2\text{-}y^2)}{}^1$. With the $4f_{x(x^2\text{-}3y^2)}$ and $4f_{y(3x^2\text{-}y^2)}$ ($m_l = \pm 3$) orbitals being strongly oblate (equatorially expanded) and $4f_{z^3}$ orbital ($m_l = 0$) being strongly prolate (axially elongated), *f*-electron density of the Er^{3+} ion is thus prolate.[5] An equatorial crystal field is the best to maximize its magnetic anisotropy. Three-coordinated, mononuclear $Er[N(SiMe_3)_2]_3$ (**1**, Figure 1), initially synthesized by Bradley and coworkers,[27] has a trigonal pyramidal symmetry, as the single-crystal X-ray diffraction studies by Herrmann and coworkers showed.[28] The Er^{3+} ion in **1** is slightly above the plane formed by the three amide ligands with C_{3v} symmetry.[28] This complex is the first reported equatorial, Er^{3+}-based SMM.[21, 29]

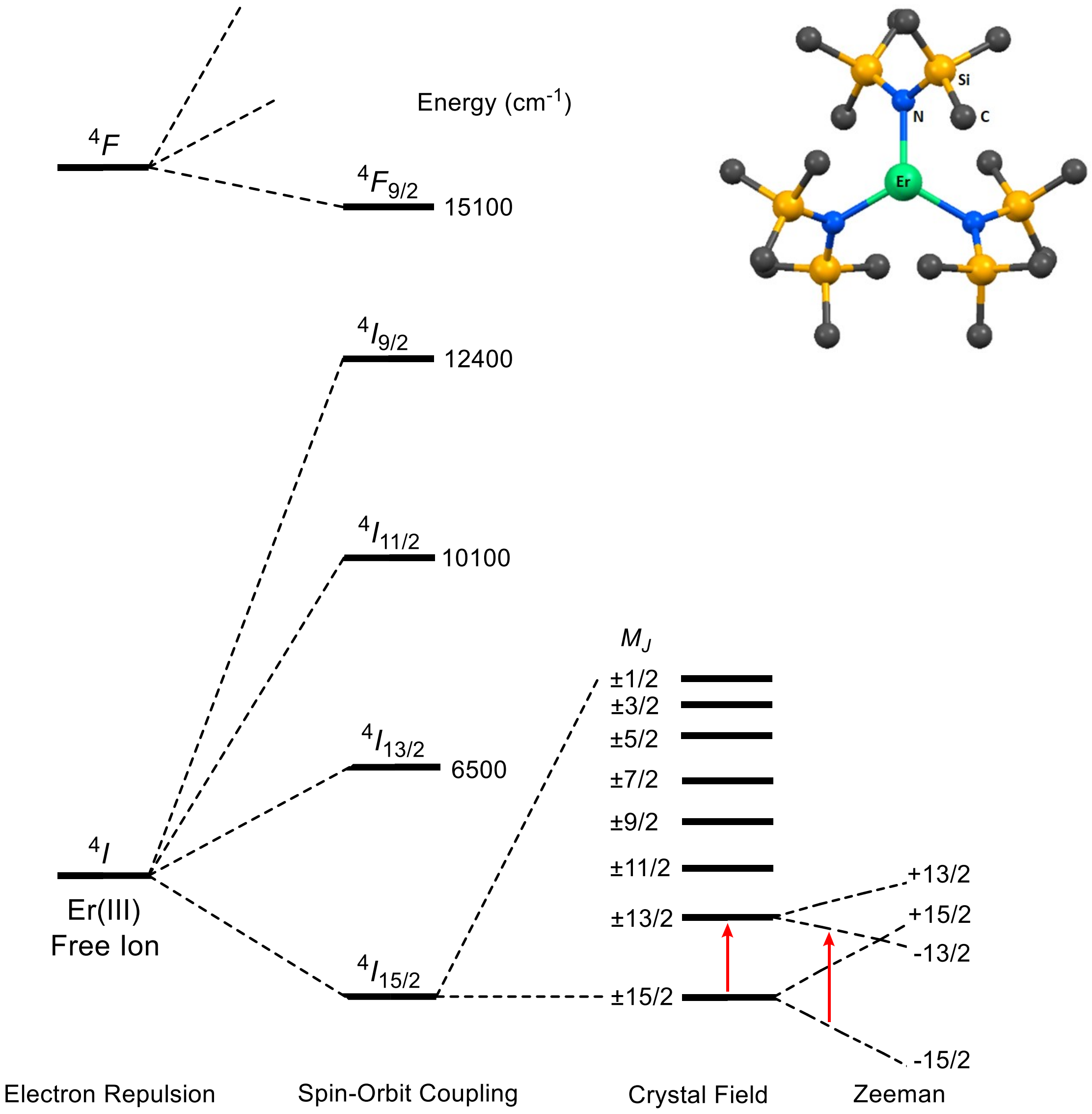

Figure 1. (Top-Right) Structure of **1**. Atom labels are Er (green), N (blue), Si (orange) and C (dark gray). (Bottom) Electronic interactions in an Er^{3+} ion due to electron repulsion, spin-orbit coupling and crystal-field contributions. Red arrows represent the relative energies of the M_J = ±15/2 → ±13/2 transition at 0 T and the -15/2 → -13/2 transition under applied magnetic fields. It should be noted that labeling the crystal-field states by a single eigenvector component M_J here is an approximation, as Jank and coworkers pointed out.[30] The labeling here does not include, *e.g.*, third-order terms in the crystal-field Hamiltonian which may mix some of the states here.

Several Er^{3+} SMMs with equatorial crystal fields have since been studied.[17-18, 20, 31] The $^4I_{15/2}$ ground manifold in the (ligand-free) Er^{3+} ion (with $2J + 1 = 16$ degenerate states) is split by the crystal field from the three amides into eight doubly-degenerate states (known as Kramers doublets) with the ground state of $M_J = \pm 15/2$, as shown in Figure 1. In the C_{3v} crystal field in **1**, the x,y directions are equal. The magnetic anisotropy of the compound is from the z direction (known as uniaxial anisotropy). Thus, complex **1** is an especially effective SIM, as the two states in $M_J = \pm 15/2$ are truly degenerate and the quantum tunneling mechanism (QTM) between them is effectively suppressed.[21]

The separations among the eight Kramers doublets, reflecting the crystal field in **1**, are fundamental properties of the compound and important to its ground-state bistability. In particular, the separation between the ground state $M_J = \pm 15/2$ and the first excited state $M_J = \pm 13/2$ is critical to SIM properties of **1**, as indicated earlier. Magnetic relaxation in **1** is believed to be mediated via a higher energy level by a thermally-activated QTM or Orbach process through an excited state.[21] To our knowledge, there have been no *direct* experimental determination of the separation. Prior to the report of SIM properties of **1** in 2014, Jank and coworkers had used a "hot-band" optical absorption technique to determine the energies of inter-Kramers transitions within the $^4I_{15/2}$ manifold, except for the $M_J = \pm 3/2$ and $\pm 1/2$ states,[30] by comparing the differences in the *visible* spectra of **1** at 5 and 50 K. For example, the ground state $M_J = \pm 15/2$ is primarily populated at 5 K, giving a peak at 650 nm for the transition from this ground state to a Kramers doublet ($M_J = \pm 7/2$) in the excited state $^4F_{9/2}$ (Figure 1). At 50 K, the first excited state $M_J = \pm 13/2$ becomes populated, i.e., both $M_J = \pm 15/2$ and $M_J = \pm 13/2$ states are now populated. The transition from the first excited state $M_J = \pm 13/2$ to the Kramers doublet $M_J = \pm 7/2$ in $^4F_{9/2}$, which has a lower energy, is possible. Thus, the visible spectrum shows a new peak (a “hot-band”) with a lower energy than the peak at 650 nm. The difference between the new peak and the 650 nm peak, 110 cm^{-1}, was treated as the separation between the ground M_J = ±15/2 and the first excited M_J = ±13/2 states.[30] However, this is an *indirect* method that is not capable of observing the inter-Kramers-doublet transitions directly, and is thus prone to some degree of error. In the SIM studies **1**, the effective barrier was determined to be 85 cm^{-1} from fitting the ln τ vs T^{-1} data (τ = relaxation time in the AC susceptibility measurement; T = temperature), quite a bit lower than the actual excited Kramers doublet, but fit well with the computed state.[21] Jank and coworkers had also calculated the first excited Kramers doublet in **1** to be 82 cm^{-1} by the simulation of the crystal-field splitting pattern.[30] Hallmen, van Slageren and coworkers have recently conducted *ab initio* calculations of the crystal-field splitting and magnetic properties of **1** by two new approaches: a combination of configuration-averaged Hartree-Fock with the techniques of local-density fitting (LDF-CAHF)[32] and a quasi-local projected internally contracted MRCI (multireference configuration interaction) approach allowing the assessment of the influence of dynamical correlation beyond second-order perturbation theory.[33] Shanmugam, Rajaraman and coworkers have used *ab initio* calculations to give the energies of the low-lying Kramers doublets and to probe the mechanism of magnetic relaxation in **1**, showing an unprecedented magnetization blockade up to the third excited state.[34] Results of the calculated levels by different methods (with a range of energies of 82 to ~112 cm^{-1} for the first excited Kramers doublet) have been compared with each other[33] and compared with the experimental results from the “hot-band” method.

Far-IR magneto spectroscopy (FIRMS) has been utilized several times to measure energy levels in lanthanide complexes, and provides a good measure of the magnetic anisotropy in the system.[35-38] Far-IR is useful for measuring magnetic transitions which are magnetic- and/or electric-dipole allowed. However, this method has rarely been used to study lanthanide-based SMMs, with most of the work performed by van Slageren et al.[39-42] High-field, high-frequency electron paramagnetic resonance (HFEPR) has a typical upper frequency limit of ~33 cm^{-1}, although a few cases exist where HFEPR has been pushed to up to 100 cm^{-1}.[43-44] Thus, HFEPR is often inadequate to study *f*-element complexes as they typically have energy levels above 100 cm^{-1}. Far-IR spectroscopy allows access to a higher energy range and is therefore a more suitable method to directly determine the magnetic energy levels in transition metal and lanthanide complexes. For complex **1** in a trigonal crystal field, all inter-Kramers transitions within the $^4I_{15/2}$ state in **1** are in theory infrared-active due to the absence of an inversion center.[45]

Another experiment technique is inelastic neutron scattering (INS), which has also occasionally been used to probe magnetic excitations in molecular *f*-element compounds.[42, 46-50] The following methods have been used to distinguish magnetic excitations in INS:[51-52] (1) Unique, different dependences of the magnetic and phonon peak intensities, respectively, on scattering angles in INS; (2) Temperature dependence;[53-54] (3) Diamagnetic controls.[46-47] It should be noted that it may be challenging to find magnetic peaks in samples with large numbers of H atoms by INS spectra from a direct-geometry spectrometer.[51] This is due to the large incoherent scattering cross-section of the H atoms, contributing to strong vibrational intensities that overshadow the magnetic excitation in INS spectra.[55] Thus, deuterated samples have sometimes been used to help reveal magnetic peaks in INS spectra,[56-57]as D atoms have a much smaller incoherent scattering cross-section. Typically, a larger amount of sample (e.g., 2.3 g of **1** in the current work and 500 mg in other studies[53-54]) is needed for INS experiments than for far-IR (5-10 mg of **1**) or Raman (one single crystal). Features of direct-geometry and indirect-geometry INS spectrometers are discussed below. It should also be pointed out that INS is an effective tool to study phonons.[58-59] Unlike IR and Raman, there is no selection rules for phonons in INS.

Phonons here refer to vibrations of molecular solids, including both external (intermolecular) and internal (intramolecular) modes. Lattice vibrations are often characterized as external modes, in which the molecules vibrate primarily as a whole with little internal distortion, including translational and librational modes.[60] Significant distortions of atoms that comprise a part of the molecule with a small displacement of the molecular center-of-mass are often called internal modes, commonly known as molecular vibrations.[61] Internal modes typically have much higher frequencies than external modes. From the perspectives of solid-state physics, the internal and external modes originate from the same governing equations, and have the same mathematical representations, meaning that both internal and external modes often couple, thus all modes are essentially mixed. Therefore, we do not attempt to distinguish internal and external modes in the current work.

Spin–phonon coupling, often called spin-lattice relaxation, is the most prevalent mechanism of magnetic relaxation in SMMs.[8, 13-14, 16, 62-67] The coupling of phonons to excited crystal-field states in lanthanide complexes may well lead to additional methods of relaxation. These spin–phonon interactions, including their nature and magnitude, are still not clearly understood. Theoretical studies have been recently conducted to understand the relationships between phonons and magnetic relaxations in SMMs.[25, 68-69] In addition, a model to calculate optical transitions from a non-degenerated electronic state to a twofold degenerated or quasi-degenerated electronic state of molecules with Jahn–Teller or pseudo–Jahn–Teller effect has been developed by Hizhnyakov and coworkers.[70-71] This method takes into account the vibronic interactions of the metal ion in a complex with two types of vibrations: local vibrations and the vibrations propagating along the crystal (phonons), leading to the symmetry-adapted ligand displacements around the metal ion as a linear superposition of normal coordinates of the local modes and phonons.[70-73] Rechkemmer and coworkers have reported spin-phonon couplings in a four-coordinate Co^{2+} SIM.[74] We have spectroscopically observed spin–phonon couplings as manifested by avoided crossings in the transition-metal SIM $Co(acac)_2(H_2O)_2$ (acac = acetylacetonate) and its isotopologues $Co(acac)_2(D_2O)_2$ and Co(acac-d_7)$_2$(D_2O)$_2$ using Raman spectroscopy, where we were able to determine the magnitudes of the couplings between the magnetic excitation and several nearby phonons.[57] Far-IR spectra (FIRMS) of $Co(acac)_2(H_2O)_2$, $Co(acac)_2(D_2O)_2$, and Co(acac-d_7)$_2$(D_2O)$_2$ show the magnetic transitions and the magnetic features of spin–phonon coupled peaks.[57] The magnetic transitions in the three Co^{2+} SMMs were also probed by INS,[75] and the effect of magnetic fields on the methyl rotation in $Co(acac)_2(D_2O)_2$ was studied.[76] INS and far-IR were also successfully used to investigate the magnetic separation in [Co(12-crown-4)$_2$](I_3)$_2$(12-crown-4) and its spin–phonon coupling.[77]

We report here comprehensive studies of **1** by FIRMS (both crystal and powder samples) and inelastic neutron scattering (INS), showing spin–phonon couplings between Kramers doublets in a lanthanide molecular complex and the IR-active phonons that, when fit with a simple model, have coupling constants ≈ 2-3 cm^{-1}. The energies of several Kramers doublets within the $^4I_{15/2}$ ground state in **1** have been directly determined using far-IR and INS spectroscopies. DFT phonon calculations have been performed and are compared with the INS spectra, providing further evidence for magnetic peak determination.

Results and Discussion

Instrumental properties and sample requirements for FIRMS and INS experiments in this study are summarized in Table 1.

Table 1. Instrumental properties and sample requirements for FIRMS and INS experiments in this study

	Features	Approximate energy ranges used (cm^{-1})	Magnets used	Temperatures (K)	Amounts of the samples used	Locations
Far-IR	Bruker Vertex 80v FT-IR spectrometer	20-700	17 T	~4.6	5-10 mg of single-crystals coated with eicosane	National High Magnetic Field Laboratory (Maglab or NHMFL)
					5-10 mg of powders mixed in eicosane	
INS by DCS[78]	Direct-geometry[51] with a monochromic incident neutron beam	~12 - ~150	10 T	1.7 K	2.3 g packed in He-filled aluminum can	NIST Center for Neutron Research (NCNR)
INS by VISION[79]	Indirect-geometry[51] with a white incident neutron beam (of all energies)	~10 to 20 (depending on the temperatures) - ~4000	No magnet	5, 25, 50, 75, 100	2.3 g (same sample as that used in DCS)	Spallation Neutron Source (SNS), Oak Ridge National Laboratory (ORNL)

Far-IR (FIRMS) Studies. Magnetic transitions in **1** were studied using far-IR with applied magnetic fields up to 17 T at 5 K using both a crystal mosaic and powder sample. When a magnetic field is applied, each Kramers doublet splits to two energy levels of $+M_J$ and $-M_J$

values (Figures 1 and S1). Depending on the temperature and relative populations, two transitions are possible between the ground and first Kramers doublet: M_J = -15/2 → -13/2 and +15/2 → +13/2. Since our far-IR experiments were conducted at 5 K, only the ground state M_J = -15/2 is expected to be populated with applied field. Thus, the M_J = -15/2 → -13/2 transition is observed. In addition, the separation between -15/2 and -13/2 states (as well as every other state in the $^4I_{15/2}$ manifold) increases with applied magnetic fields. Thus, the transition shifts to higher energies. When the sample is a crystal, the observed transitions are due to single orientations of magnetic field with respect to the magnetic anisotropy. In powder samples, the spectra are an average of all orientations and the magnetic transition thus has a tendency to broaden instead of remaining as a clear discrete peak.

Intra-manifold far-IR transitions between crystal-field split states stemming from a single *J*-level (Figure 1) have been studied for many systems, although selection rules for such transitions have yet to be discussed.[80-82] Instead, they are often assumed to be purely magnetic dipole-allowed. Inter-manifold transitions have more well-defined selection rules, and in non-centrosymmetric systems are allowed by induced electric-dipoles due to mixing of *d* and *f* states.[80]

Upon the application of field, three far-IR excitations sensitive to magnetic fields appear at 104 cm^{-1} and 245 cm^{-1}, referred to henceforth as ν_1 and ν_3, respectively (Figures 3 and 4 for crystal and powder samples, respectively). A transition between these two is present in the powder spectra at ~180 cm^{-1}, labeled as ν_2 (Figure S5). All three excitations appear to shift to higher energies with applied magnetic field. In the crystal sample, the magnetic transitions are weak compared to the corresponding excitations in the powder samples. However, all data are consistent. It should be noted that these magnetic peaks exist largely as shoulders or very weak bands in the far-IR spectra. The intense peaks indicated by the dashed red lines in Figure 3 are phonons. The ν_1 transition (assigned to the $M_J = -15/2 \rightarrow -13/2$ transition[30]) is in close agreement with the INS data (*vide infra*). The three peaks agree reasonably well with previously reported data from indirect measurements,[30] with the next two excitations ν_2 and ν_3 assigned as transitions from the ±15/2 ground state to the ±11/2 and ±9/2 excited states, respectively.

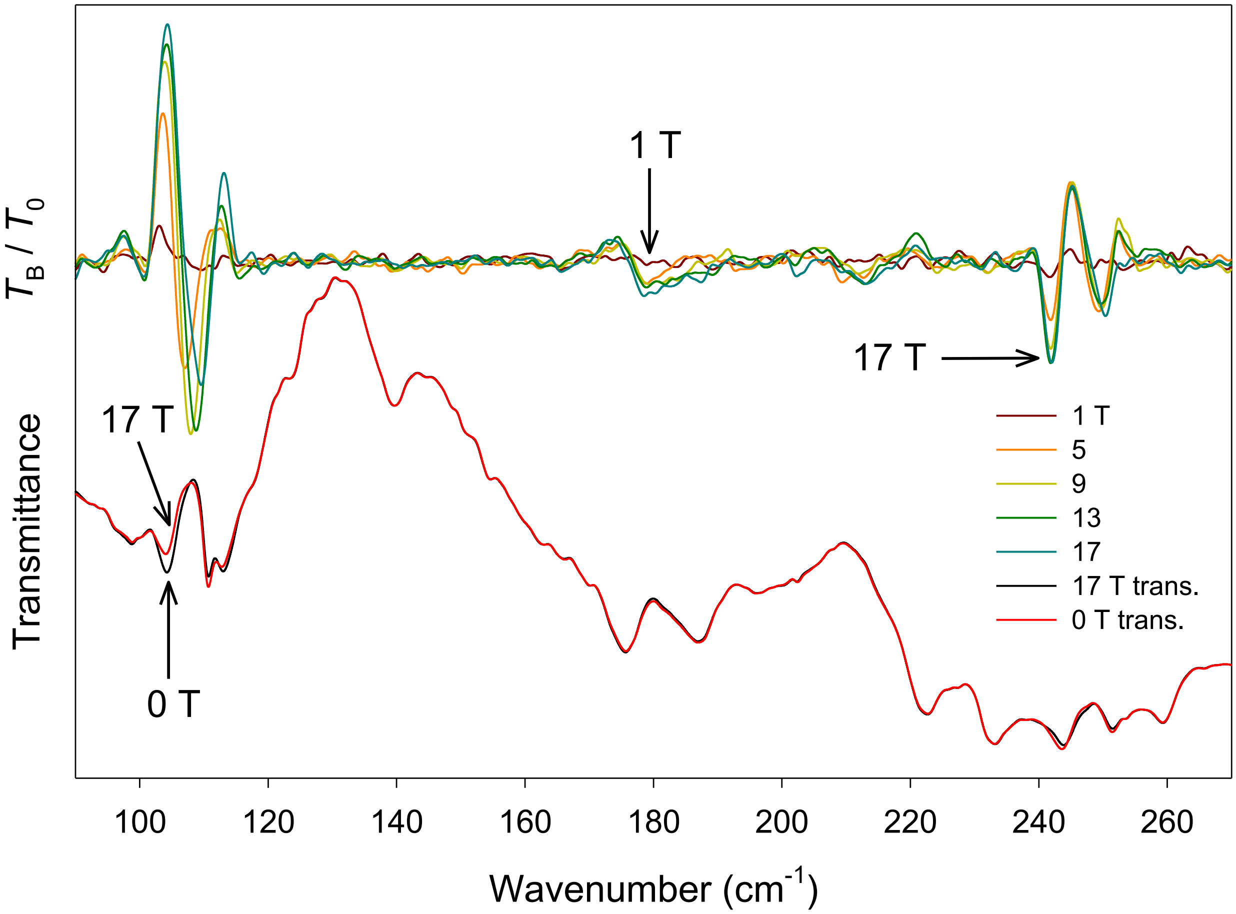

Figure 2. (Bottom) Far-IR transmission spectra of a crystal sample of **1** at 0 T (black) and 17 T (red); (Top) Transmission normalized to the zero-field spectrum T_B / T_0 at 1, 5, 9, 13, and 17 T.

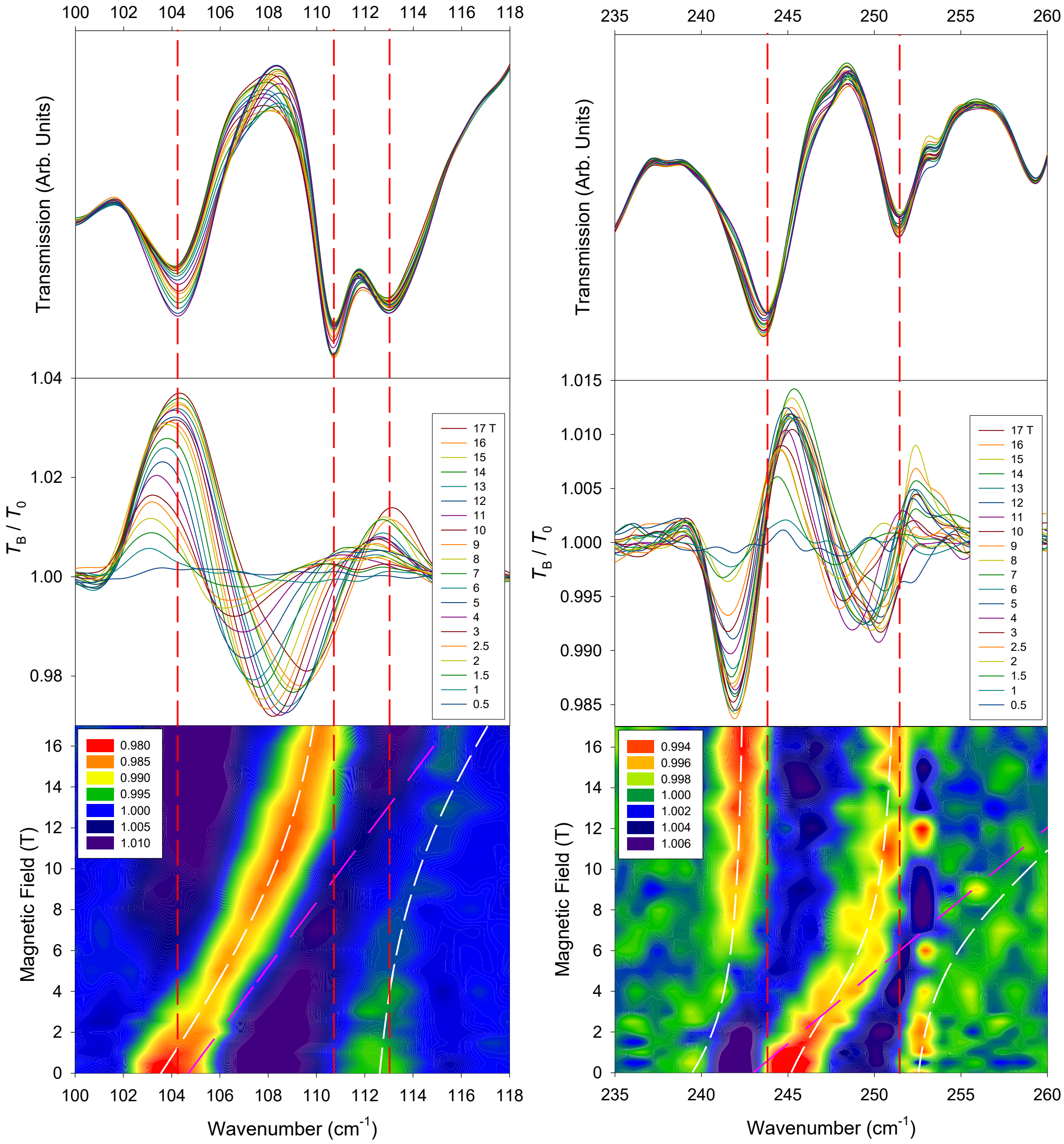

Figure 3. Far-IR spectra in the vicinity of magnetic excitations (Left) ν_1 and (Right) ν_3 in a crystal sample of **1**. (Top) Raw transmission; (Middle) Transmission (T_B) normalized to the zero-field spectrum (T_0); (Bottom) Contour plot of the normalized transmission (by average). White lines represent results of the spin–phonon coupling fit. Pink lines represent the shift of the uncoupled magnetic peak used for the coupling parameters E_{sp}. Vertical red lines indicate approximate zero field positions of dominant phonon excitations.

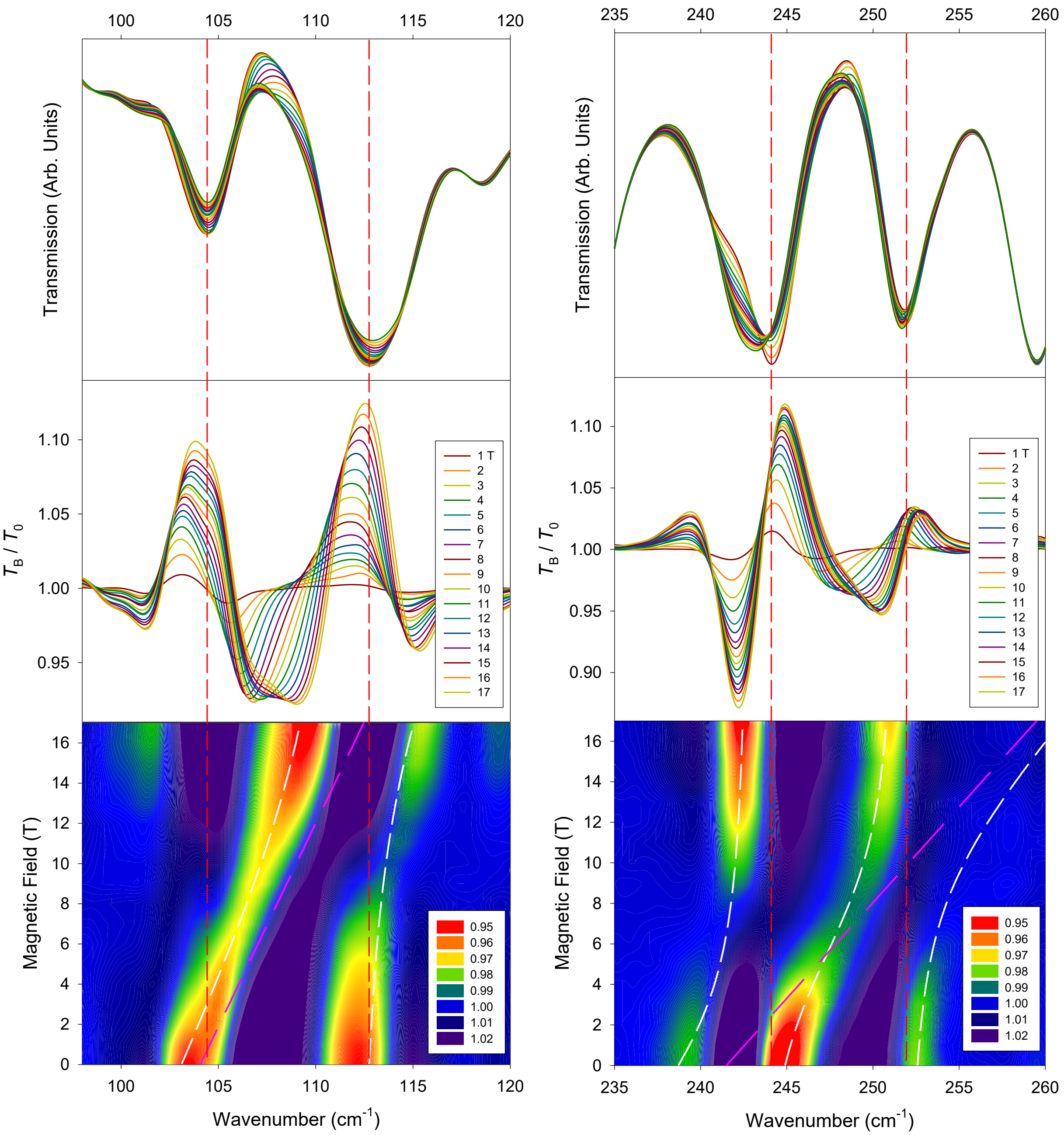

Figure 4. Far-IR spectra in the vicinity of magnetic excitations (Left) ν_1 and (Right) ν_3 in a powder sample of **1**. (Top) Raw transmission; (Middle) Transmission (T_B) normalized to the zero-field spectrum (T_0); (Bottom) Contour plot of the normalized transmission (by average). White lines represent results of the spin-phonon coupling fitting. Pink lines represent the shift of the uncoupled magnetic peak used for the coupling parameters E_{sp}. Vertical red lines indicate approximate zero field positions of dominant phonon excitations.

Spin–phonon couplings and shift paths are revealed upon close examination of the contour plots of the normalized spectra (Figures 3, 4 and 4), although a visual inspection of the raw transmittance data (Figure 3-Top) does not indicate obvious couplings or where peaks are shifting. We speculate that either each of these magnetic excitations or the phonon that they interact with is very weak. A symmetry analysis indicates that a transition from the $M_J = \pm 15/2$ ground state ($\Gamma_{5/6}$ and $E_{3/2}$ in Bethe's and Mulliken's notation, respectively) to any other excited crystal-field state (either $\Gamma_4/E_{1/2}$ or $\Gamma_{5/6}$ in C_{3v}) should be electric or magnetic dipole-allowed in far-IR spectroscopy in the z ($\Gamma_{5/6}$) and x-y (Γ_4) directions.[30, 45, 83-84] Both ν_1 and ν_3 experience couplings with at least one observed adjacent phonon (Figure 3).

The ν_1 peak is coupled with a phonon at approximately 112 cm^{-1} (Figure 3-Left), causing it to broaden and lose intensity. In other words, both states of the two spin-phonon coupled peaks in Figure 3-Left Bottom contain magnetic and phonon features. Since the phonon here is far-IR-active, the phonon portions of both peaks contribute to the observation of the two peaks. The magnetic transition ν_1 is assigned to be at 104 cm^{-1}, instead of the 112 cm^{-1} peak, as ν_1 agrees well with the INS results discussed below. In addition, the 104 cm^{-1} peak shifts linearly for the majority of the fields measured, but experiences what appears to be an avoided crossing at higher fields. However, the 17 T part of the lower branch in Figure 3-Bottom Left, at ~110 cm^{-1}, is not directly on top of the 0 T part of the upper branch at ~112 cm^{-1}. The observation suggests the following: (a) A higher magnetic field (such as 35 T) may be needed to make the high-field part of the lower branch to be on top of the 0 T part of the upper branch; (b) There is second-order vibronic coupling here, which may shift the first excited state Kramers double $M_J = \pm 13/2$ with the magnetic fields (before the Zeeman effect). The shifts of both the lower and upper branches in Figure 3-Bottom Left may be explained by the second-order vibronic coupling. Or both avoided crossing and second-order vibronic coupling perhaps contribute the observed spin-phonon coupling here. Understanding the nature of the spin-phonon coupling here is difficult as the Er^{3+} center in the crystal structure is disordered in two positions.[28, 30] The disorder prevents the interpretation of the results, including the development of a vibronic coupling model for **1**, as done earlier for $Co(acac)_2(H_2O)_2$.[57]

If the second-order vibronic coupling is ignored, the coupling in Figure 3-Left may be modeled by Eq. 1 consisting of a 2 × 2[57] matrice:

$$H = \begin{pmatrix} E_{sp} & \Lambda \\ \Lambda & E_{ph} \end{pmatrix} \tag{1}$$

where E_{sp} and E_{ph} are the expected energies of the magnetic and phonon peaks, respectively, prior to coupling; Λ represents the spin–phonon coupling constant. Solving the matrix in Eq. 1 gives two eigenvalues $E_{\pm}$ (with the avoided-crossing peaks) in the secular Eq. 2. Since Eq. 2 involves Λ^2, the sign of Λ may not be determined from the far-IR spectra here.

$$\begin{vmatrix} E_{\mathrm{sp}} - E_{\pm} & \Lambda \\ \Lambda & E_{\mathrm{ph}} - E_{\pm} \end{vmatrix} = 0 \tag{2}$$

Upon coupling, one state shifts to higher E_+ while the other shifts to lower E_-.[85] Fitting the data in Figure 3-Left by Eq. 2 yields $|\Lambda| = 3.0(3)\ \mathrm{cm}^{-1}$ with fitting parameters in Table S1.[86]

If the second-order vibronic coupling is included in the consideration, the spin peak position (the lower branch) in Figure 3-Bottom Left may be represented by

$$E_{sp} = E_0 + CB \tag{3}$$

where E_0 is the peak of the magnetic transition at 0 T (104 cm^{-1}); B is the magnetic field; C is a constant. Eq. 2 thus becomes

$$\begin{vmatrix} (E_0 + CB) - E_{\pm} & \Lambda \\ \Lambda & E_{\mathrm{ph}} - E_{\pm} \end{vmatrix} = 0 \qquad (4)$$

Fitting the data in the spectra in Figure 3-Left by Eq. 4 yields $|\Lambda| = 2.4(6)$ cm^{-1} and $C = 0.59(5)$ cm^{-1}/T.

The ν_3 peak at 245 cm^{-1} (Figure 3-Right) for the $M_J = \pm 15/2 \rightarrow \pm 9/2$ transition at 0 T, shows similar features, except that it lies between two phonons that it is coupled with *simultaneously*. As ν_3 shifts to higher energies, a lower energy excitation appears at 242 cm^{-1} at higher fields, originating from ~238 cm^{-1} due to coupling with the magnetic peak. At the higher magnetic fields of 12-17 T, the intensity of this peak significantly increases due to decreasing spin–phonon coupling with the magnetic peak, essentially regaining its original intensity from ν_3. It is likely that the magnetic portion of the excitation is inherently weak in far-IR, and is only viewed due to its coupling to phonon transitions, essentially “stealing” their intensity, as observed in Raman spectra of $\mathrm{Co(acac)_2(H_2O)_2}$.[57] Thus, the 253 cm^{-1} excitation becomes too weak to observe after approximately 4 T. If the second-order vibronic coupling is ignored, these three excitations were modeled using a 3 × 3 matrix in Eq. 5 similar to that in Eq. 1.

$$H = \begin{pmatrix} E_{sp} & \Lambda_2 & \Lambda_3 \\ \Lambda_2 & E_{ph2} & 0 \\ \Lambda_3 & 0 & E_{ph3} \end{pmatrix} \qquad (5)$$

where E_{sp} is the energy value for an uncoupled ν_3 excitation; E_{ph1} and E_{ph2} are energies of the two phonons; Λ_1 and Λ_2 are spin-phonon coupling constants with phonons 1 and 2, respectively.

The fitting of the data in Figure 3-Right yields $\Lambda_2 = 3.0(5)$ cm^{-1} and $\Lambda_3 = 3.0(7)$ cm^{-1} with fitting parameters in Table S1.[86] If the coupled phonons around ν_3 are instead individually modeled using two separate 2 × 2 matrices (Figure S6), the coupling constants are about the same. If the second-order vibronic coupling is included in the fitting here, as in Eqs. 3 and 4 for the first magnetic transition, the spin-phonon coupling constants Λ_2 and Λ_3 are expected to be smaller. For ν_2 ($M_J = \pm15/2 \rightarrow \pm11/2$ at 0 T, Figure S5) at ~180 cm^{-1}, the changes with fields are small relative to those of ν_1 and ν_3. The intense phonon at 176 cm^{-1} shifts very slightly to higher energies, likely relaxing back into a pure phonon when ν_2 shifts away. Earlier, the $M_J = \pm15/2 \rightarrow \pm11/2$ transition ν_2 was calculated to be at 145 cm^{-1} and indirectly observed at 190 cm^{-1} by the "hot-band" technique.[30] Due to the complex structure of the contour plot in Figure S5, it is difficult to say with certainty where the origin of the magnetic peak ν_2 lies. Here, we see a blue region shifting to higher energies, which should correspond to the movement of a valley or a lower-energy excitation. This blue region shifts about 12 cm^{-1}, which is a similar order of magnitude compared to the shifts of ν_1 and ν_3. Thus, it is reasonable to assign the inter-Kramers-doublet transition ν_2 as being ~180 cm^{-1} (estimated error: 5 cm^{-1}) at 0 T. **Inelastic Neutron Scattering (INS) Studies.** Two INS studies, one using Disk Chopper Spectrometer (DCS)[78, 87] with variable magnetic fields at the NIST Center for Neutron Research (NCNR) with a 10 T magnet and another using Vibrational Spectrometer (VISION)[79, 88] with variable temperatures at Spallation Neutron Source (SNS), Oak Ridge National Laboratory (ORNL), were conducted for **1** mainly to observe the $M_J = \pm15/2 \rightarrow \pm13/2$ magnetic transition. In addition, VISION spectra give phonons of **1** by INS that are compared with calculated phonons. We have recently reviewed neutron instruments, including DCS and VISION, for research in coordination chemistry.[51]

Each molecule of $Er[N(SiMe_3)_2]_3$ (**1**) has 54 H atoms. Hydrogen atoms give strong incoherent neutron scattering, leading to background noise in direct-geometry INS spectra.[55] Thus, it is particularly challenging to study the magnetic excitations in **1** in INS by DCS. It should be pointed out that, to our knowledge, perdeuterated ligand $-N(SiMe_3\text{-}d_9)_2$ or $Er[N(SiMe_3\text{-}d_9)_2]_3$ (**1-*d*$_{54}$**) has not been reported.

As a direct-geometry spectrometer,[60, 78, 87, 89] DCS uses multiple choppers to produce a pulsed *monochromatic* neutron beam at the sample. Time-of-flight analyses of scattered neutrons determine energy transfers E between the incident neutron and the sample as well as scattering-vector $\boldsymbol{Q}$.[51, 75, 78, 87] DCS is limited to energies less than ca. 150 cm^{-1}. One feature relevant to the current research is that a 10 T magnet could be used in DCS, although the magnet itself blocks a number of detectors leading to the decrease in signal/noise ratios.[75]

At 0 T, we observed the magnetic transition ν_1 in **1** from the ground ($M_J = \pm 15/2$) to the first excited state ($M_J = \pm 13/2$) at 104 cm^{-1} at 1.7 K. Since the INS experiment was conducted at 1.5 K, only the ground state $M_J = -15/2$ is expected to be populated (Figures 1 and S1). Thus, only the $M_J = -15/2 \rightarrow -13/2$ transition is expected. In addition, the separation between -15/2 and -13/2 states increases with applied magnetic fields (Figure 5). Thus the $M_J = -15/2 \rightarrow -13/2$ transition/peak shifts to higher energies with applied magnetic fields. This observation is consistent with those from far-IR. At 5 T, the magnetic peak shifted to 105.1 cm^{-1} in INS (Figure 5). The phonons in the region do not seem to be affected by the application of magnetic fields. At 10 T, the magnetic peak further shifted into the shoulder of a phonon peak, and its energy position could not be accurately determined (Figure 5). However, both the area and full-width-at-half maximum (FWHM) of the phonon peak increased at 10 T due to the overlap with the magnetic peak (Table S2).

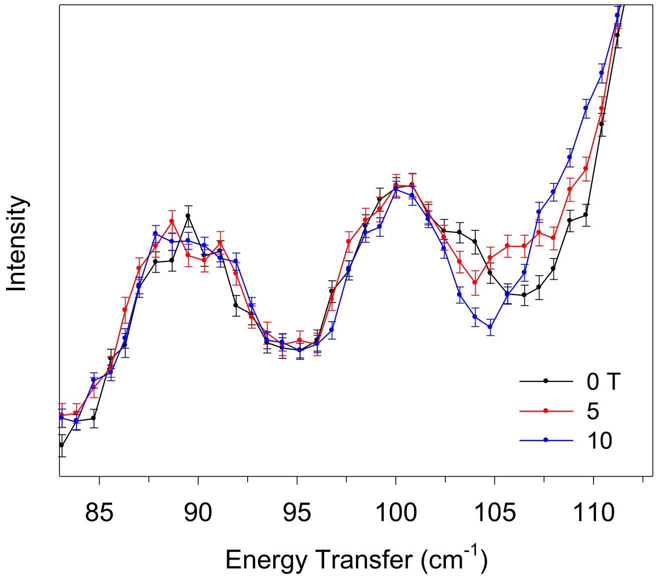

Figure 5. INS spectra (DCS) at 1.7 K at 0 (black), 5 (red), and 10 T (blue). Error bars indicate ±1σ. The spectra in the complete energy transfer range (10-140 cm^{-1}) and a contour plot of the normalized scattering intensity (by average) are given in Figure S9. Unlike the transmittance far-IR spectra in Figures 2-3 and S3-S5, INS peaks in Figures 4-7 are pointed upward.

Unlike DCS, VISION is an inverse-geometry INS spectrometer.[51, 60, 75, 79, 88-89] Pulsed, white-beam incident neutrons (with different energies) at high flux are scattered by the sample and then focused onto detectors by crystal analyzer arrays. Such inverse-geometry INS spectrometers typically offer improved signal-to-noise ratio.[51] For example, the overall inelastic count rate at VISION is more than two orders of magnitude higher than other similar spectrometers.[79] Currently VISION is *not* equipped with an electromagnet.

INS spectra at the VISION *without* magnetic field (Figure 6) are similar to the INS spectrum at 0 T at DCS (Figure 5). The magnetic peak at 104 cm^{-1} is visible on the shoulder of a phonon peak at 5 and 25 K. The magnetic peak is expected to disappear with increasing temperatures as Boltzmann statistics predicts. Indeed, the spectra in Figure 6 show the magnetic peak ν1 at 104 cm^{-1} disappears by 100 K. Here, Bose correction is used to treat the INS data from VISION. Phonons and electrons are bosons and fermions, respectively, and thus follow Bose–Einstein statistics and Fermi–Dirac statistics, respectively.[75, 90] The Bose correction applies a frequency- and temperature-dependent normalization factor such that INS spectra measured at different temperatures are brought to a similar level for comparison. The Bose-corrected spectra at different temperatures are expected to have similar profile and baseline intensity. The magnetic transition, which does not follow the expected temperature dependence for phonons, will be highlighted for identification. Another feature of VISION is that there are two banks of analyzers with two different scattering angles (represented by $|\boldsymbol{Q}|$ = magnitude of the neutron momentum transfer during the scattering process;[51] $|\boldsymbol{Q}|$ is sometimes represented as Q), one at 45° (forward scattering, lower $|\boldsymbol{Q}|$) and another at 135° (backscattering, higher $|\boldsymbol{Q}|$) giving two spectra per experimental data acquisition.[51] Magnetic peaks are stronger at small scattering angles (in forward scattering spectra) in INS.[52] Thus, the forward scattering spectra at VISION are shown in Figure 6.

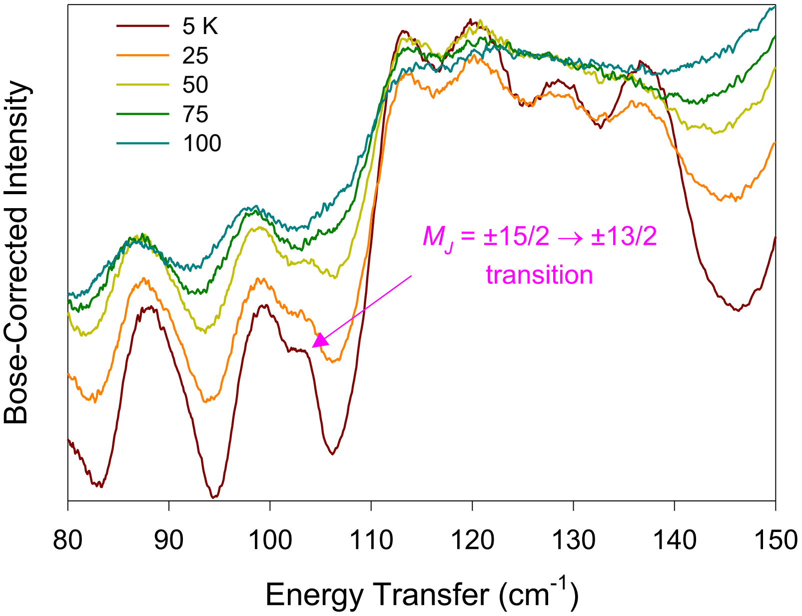

Figure 6. Bose-corrected VT INS spectra of **1** from the forward scattering at VISION.[51, 79]

Phonon Calculations and Comparison with Spectra. Phonons in **1** have been calculated by a periodic DFT method offered by VASP (Vienna Ab initio Simulation Package).[91] The calculated phonons may be compared with those from INS experiments. In order to better understand the INS spectra, it is important to be able to assign the peaks to certain vibrational or magnetic excitations. DFT allows first-principle prediction of interatomic force constants and phonons from electronic structure calculations. INS spectra due to vibrational (nonmagnetic) excitations can then be simulated using the phonon information. Technical details of the calculation can be found in the Experimental Section. The calculated phonons may be compared with those from INS experiments.

In addition to probing magnetic transitions, INS is an effective tool to probe phonons, including intramolecular vibrations. Unlike optical vibrational spectroscopies such as IR and Raman which are governed by different selection rules, INS does not have selection rules for phonons, as it is based on the kinetic energy transfer between the incident neutrons and the sample.[51, 59, 89] Using INS to probe phonons has been reviewed by Hudson.[59] By comparing the computed phonon spectra with the experimental INS spectra, magnetic peaks that are *not* in the computed spectra may be revealed.

The reported crystal structure of **1** displays a disorder with the Er^{III} ion on both sides of the plane formed by the three amide ligands.[28] It is not clear if the disorder is static (C_{3v} symmetry of the complex) or dynamic (D_{3h} symmetry). We have performed DFT calculations to address this issue. Configurations with the Er^{III} ion on the two different positions were first relaxed to the potential energy minimum. It is found that the separation of the two sites is about 1.5 Å. The potential energy barrier between the two sites was further calculated to be about 250 meV (2016 cm^{-1}) using the nudged elastic band method.[92] These results suggest that the disorder of the Er^{III} ion is static for the following: (1) Er is a heavy element, the probability of quantum tunneling over 1.5 Å is essentially zero; (2) The energy barrier is substantially higher than what thermal activation can overcome (with non-negligible probability) at any relevant temperature.

The phonon density-of-states from INS of **1** seems to match well with those calculated across the entire range, as shown in Figures 7 and 8. A complete list of calculated phonons (for both forward- and back-scattering INS) and their symmetries are given in Table S2. The exact positions of the phonons are, however, difficult to calculate, especially at low energies. It should be noted there are no shoulder peaks representing the magnetic excitation that are calculated, providing further evidence to its nature as a magnetic transition. However, while this supports the assignment of the $M_J = \pm 13/2$ peak, there are little to no indications of any further magnetic peaks in INS. The calculations are expected to help assign the peaks in INS and far-IR spectra.

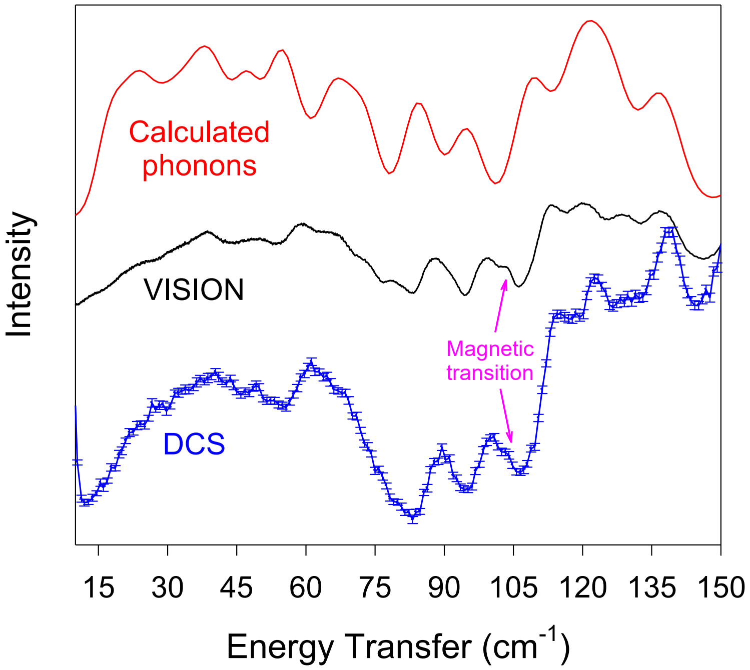

Figure 7. Calculated and experimental INS spectra of **1** at 5 K in the 0-150 cm^{-1} range. (Top) Calculated phonons; (Middle) VISION spectrum at 0 T; (Bottom) DCS spectrum at 0 T.

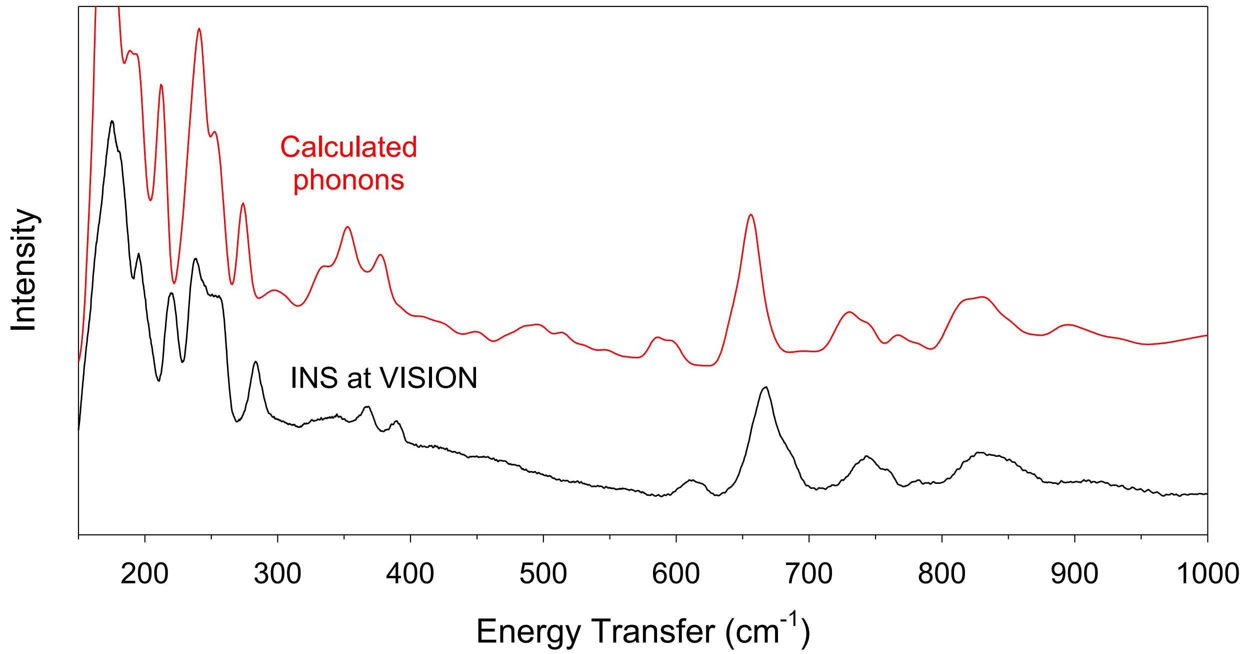

Figure 8. INS spectrum (VISION) at 5 K in the 150-1000 cm^{-1} range in comparison with the calculated phonons. The 1000-3600 cm^{-1} range is given in Figure S11. Calculated excitation intensities of the entire range are shown in Figure S12. Calculated phonons in **1**, including their symmetries and intensities, are given in Table S3.

Comparison of the Far-IR and INS Results. Results from far-IR and INS in the current work are compared with the previously reported values by the "hot band" method in Table 2.[30]

Table 2 Energies of each magnetic/inter-Kramers-doublet transition[a]

Transition	**Energy (cm^{-1}) by the "hot band" method[30]**	**Energy (cm^{-1}) from the current work[b]**
±15/2 → ±13/2 (ν_1)	110 cm^{-1}	104 cm^{-1} (far-IR/INS)
±15/2 → ±11/2 (ν_2)	190 cm^{-1}	Approximate 180(5) cm^{-1} (far-IR)
±15/2 → ±9/2 (ν_3)	245 cm^{-1}	245 cm^{-1} (far-IR)

[a] The ±15/2 → ±7/2 transition (ν_4), observed at 327 cm^{-1} by the indirect "hot-band" optical absorption technique, appears to be at 285 cm^{-1} in FIRMS spectra (Figure S7).

[b] The errors for the energies are estimated to be ca. 1 cm^{-1} (Supporting Information).

The first inter-Kramers transition peak ν_1 is weak relative to the overlapping phonon, making a direct observation of the peak and its spin–phonon couplings in transmittance far-IR spectra (Figures 2 and S3) difficult. However, the far-IR contour plots (Figures 3 and 4 Bottom-Left) clearly reveal the presence of a shifting peak and its spin–phonon coupling with an adjacent phonon as avoided crossing. The third inter-Kramers transition peak ν_3 is much more pronounced at 0 T, residing close to a phonon in transmittance far-IR spectra (Figures 3 and 4 Top-Right), and its spin–phonon couplings with adjacent phonons are clear in the far-IR contour plot (Figures 3 and 4 Bottom-Right). The couplings may somewhat alter the positions of ν_1 and ν_3 and the neighboring phonons from their ground state energies. In magneto-INS at DCS (Figure 5), the magnetic peak is more obvious than in the transmittance far-IR in Figures 2 and S3, and, shifting the transition with fields, the peak was identified. In the current studies, DCS probes energy transfers less than 140 cm^{-1} and thus, it was not used to probe ν_2 at ~180 cm^{-1}, ν_3 at 245 cm^{-1}, or any subsequent magnetic excitation. The spin–phonon coupling may also not be observable with only a 10 T field (used in INS), as the far-IR contour plot (Figures 3 and 4 Bottom-Left) shows that 10 T is not sufficiently strong to shift the magnetic peak close enough to the phonon to reveal the coupling. It should be pointed out that the far-IR spectrometer used in the current work is coupled to a 17 T magnet.[93] The large magnet in such a sample environment does not block the far-IR detector. In contrast, the sample environment for neutron scattering with the 10 T magnet at DCS requires the placement of the magnet in front of a large number of the detectors,[78] thus blocking the detectors and reducing the signal/noise ratios of the peaks.[75] Therefore, for the magneto-INS studies at DCS, we focused on locating the magnetic/inter-Kramers transition ν_1. In addition to direct-geometry DCS with fixed, selected incident energy E_i and a wide range of $\boldsymbol{Q}$ measurement, indirect-geometry VISION with a "white" incident beam with a much larger flux of the incident neutron beam[51, 79] gives a wide energy transfer range with high resolution, albeit limited $\boldsymbol{Q}$ information. Although VISION is *not* currently equipped with a magnet, Bose-corrected VT INS spectra in Figure 6 support the assignment of the magnetic transition ν_1 at 104 cm^{-1}.

Magneto-Raman spectroscopy was used to study **1**, but it did not reveal the magnetic peaks, as shown in Figure S10 and discussed in the SI. It is possible the air-sensitivity or fluorescence of the sample may have played a role in reducing the effectiveness of the technique. When a vibration (or phonon) leads to a polarizability change in a molecule, the transition is Raman active. Similarly, if an electronic (or magnetic) transition leads to a polarizability change in a molecule, the transition is also Raman active.[94] The selection rules for electronic Raman transitions are: $\Delta J \leq 2$, $\Delta L \leq 2$, $\Delta S = 0$.[94-96] However, these rules are likely relaxed under applied magnetic fields due to crystal strain.[96] Intra-manifold transitions in lanthanide compounds have been studied by Raman in the past.[94]

Conclusion

The current work reports the ~~first~~ observation of spin–phonon couplings in a lanthanide molecular complex, which are observed as avoided crossings in FIRMS with coupling magnitudes ≈ 3 cm^{-1}. In addition, far-IR and INS spectroscopies have been used to quantify the magnetic/Kramers doublet levels in the trigonal pyramidal Er^{3+} compound. They help piece together a picture of these magnetic energy levels and the couplings they experience with neighboring phonons. The studies here are expected to help understand magnetic properties of the SIM, including its magnetic relaxations. We believe the current approach with various complimentary spectroscopies could be utilized in the studies of similar *f* complexes with first-order spin-orbit couplings, assigning inter-Kramers transitions and revealing previously unknown spin–phonon couplings. While transitions such as these are not normally expected in corresponding transition metal SIMs without M_J states due to possessing quenched first-order angular momentum, we believe that any complex with significant spin-orbit couplings should display these transitions in optical spectroscopies.

Experimental Section

1 was synthesized according to a previously reported method.[21, 27-29] Instrumental properties and sample requirements for the experiments in this study are summarized in Table 1.

Far-IR Magneto Spectroscopy (FIRMS). Far-IR spectroscopic studies were conducted at the National High Magnetic Field Laboratory (NHMFL) at Florida State University. For far-IR spectra, the powdered samples dispersed in eicosane in an argon glovebox. Crystal samples were mounted as a mosaic of several needle-like crystals and coated with eicosane in the glovebox to minimize reaction with air when the sample was later loaded into the 17 T magnet. Spectra were collected at ~4.6 K using a Bruker Vertex 80v FT-IR spectrometer coupled with a 17 T superconducting magnet.

Unlike Raman crystal samples, far-IR samples could be easily mounted in the glove box and coated with eicosane, as far-IR measures the bulk of the crystal. Since Raman is a surface scattering technique, mounting air-sensitive samples is currently very difficult since the crystals cannot be coated with eicosane without reducing the effectiveness of the technique.

INS with Variable Fields and Temperatures. Two INS studies using different instruments were conducted: (a) Variable-magnetic-field (0 to 10 T) INS spectra of **1** at 1.7 K at the time-of-flight DCS at NIST Center for Neutron Research (NCNR). This study leads to the identification of the first excited magnetic level with magnetic fields. (b) Variable-temperature INS spectra of **1**, without a magnet, at VISION at Oak Ridge National Laboratory (ORNL). Both studies used the same powder sample.

At DCS,[87] a 10 T vertical magnet with a dilution refrigerator was used as the sample environment. Inside a helium glovebox, polycrystalline solid of **1** (2.3 g) was put on a piece of aluminum foil, rolled into a cigar shape, and then wedged and sealed inside an aluminum sample holder so the sample would not move with applied field. Data were collected at 1.7 K with an incident energy of E_{i} = 201.6 cm^{-1} (wavelength of 1.81 Å) at 0 T, 5 T, and 10 T. In addition, data at 20 K at 0 T were collected but no significant difference between the spectra at 1.5 and 20 K (0 T) was observed. At DCS, data were collected up to ca. 150 cm^{-1}. All data processing was completed with Data Analysis and Visualization Environment (DAVE).[97] These INS experiments are particularly challenging, as the distance between the split magnet coils necessitates a smaller neutron beam, leading to reduction of the incident beam size by a factor of 2.5 and a concomitant shadowing of detectors, giving ~33% detector efficiency compared to operations with sample environments such as a cryostat.

After the DCS experiment, the aluminum sample holder was shipped from NCNR to ORNL for variable-temperature INS at VISION. The INS spectra of **1** were measured at 5, 25, 50, 75, and 100 K for 1 h at each temperature without magnetic field. VISION,[88] an indirect-geometry instrument,[51] provides data up to 4000 cm^{-1}. The indirect-geometry design at VISION offers two banks of detectors for both forward (low $|\boldsymbol{Q}|$) and back (high $|\boldsymbol{Q}|$) scattering of neutrons.[88] The phonon population effect was corrected by normalizing the INS intensity at energy transfer ω with coth ($\hbar\omega/2kT$) ($\hbar$ = reduced Planck's constant; k = Boltzmann constant).[58]

VASP Calculation. Complex **1** crystallizes in space group P-31c (No. 163) and has trigonal D_{3d} symmetry.[98] VASP[91] calculations on **1** were conducted. Geometry optimizations were performed based upon the single-crystal X-ray structure of **1** determined at 293 K. The optimized structure was used for the phonon calculations. Spin-polarized, periodic DFT calculations were performed using VASP with the Projector Augmented Wave (PAW)[99-100] method and the Generalized Gradient Approximation (GGA)[101] exchange correlation functional, with a Hubbard U parameter of 6.5 eV.[102-103] Energy cut off was 800 eV for the plane-wave basis of the valence electrons. Total energy tolerance for electronic structure minimization was 10^{-8} eV. The optB86b-vdW non-local correlation functional that approximately accounts for dispersion interactions was applied.[104] For the structure relaxation, a 2 × 2 × 4 Monkhorst-Pack mesh was applied. Phonopy,[105-106] an open source phonon analyzer, was used to create the 1 × 1 × 2 supercell structure and extract symmetries. VASP was then employed to calculate the force constants on the supercell in real space using DFT. Phonopy was not able to assign the doubly-degenerated E vibrations for **1**. Thus, the calculated E phonons are labeled as both g and u in Table S2.

Associated Content

Supporting Information

The following are provided: (1) Zeeman splitting of the $M_J = \pm 13/2$ and $\pm 15/2$ levels under applied magnetic fields calculated with g = 1.2 (Figure S1); (2) Image showing crystals used in far-IR measurements (Figure S2); (3) Contour plot showing the spin–phonon coupling model for ν_3 in far-IR by two separate 2 × 2 matrix equations (Figure S6); (4) Additional spectra, including far-IR (Figures S3-S7), INS (Figures S8-S9), and Raman (Figure S10); (5) INS spectrum in the 1000-3600 cm^{-1} range in comparison with calculated phonons (Figure S11); (6) Calculated backscattering INS spectrum and peak intensities (Figure S12); (7) Table S2 listing the area and FWHM (full width at half maximum) of the phonon peak in INS from DCS at 115 cm^{-1} at 10 T; (8) Table S3 listing calculated phonons in $Er[N(SiMe_3)_2]_3$ (**1**). The Supporting Information is available free of charge on the ACS Publications website at DOI:

Author Information

Corresponding Author

*E-mail: xue@utk.edu

Authors Contributions

D.H.M., M.O. and D.S. performed the far-IR experiments and interpreted the data. S.E.S., C.M.B., Y.C., L.L.D. and A.J.R.C. conducted the INS experiments and interpreted the data. S.E.S. and Y.C. performed and analyzed the DFT phonon calculations. D.H.M., K.T., D.S., R.R., G.K. and Z.L. conducted the Raman experiments and interpreted the data. Z.Z., M.G. and J.T. synthesized and characterized the compound **1** and grew its crystals for the studies. Z.L.X. designed and supervised the research and helped analyses of the results. D.H.M., S.E.S. and Z.L.X. wrote the manuscript with input from all authors.

Notes

The authors declare no competing financial interest.

Acknowledgments

The authors thank financial support by the US National Science Foundation (CHE-1633870 and CHE-1900296 to Z-L.X.), U.S. Department of Navy HBCU/MI program (K.T.), and a Shull Wollan Center Graduate Research Fellowship (S.E.S). Acknowledgment is also made to the Donors of the American Chemical Society Petroleum Research Fund for partial support of this work. A portion of this work was performed at the National High Magnetic Field Laboratory which is supported by National Science Foundation Cooperative Agreement No. DMR-1644779 and the State of Florida. Neutron scattering experiments were conducted at the VISION beamline at ORNL's Spallation Neutron Source, which is supported by the Scientific User Facilities Division, Office of Basic Energy Sciences (BES), U.S. Department of Energy (DOE), under Contract No. DE-AC0500OR22725 with UT Battelle, LLC. The computing resources were made available through the VirtuES and the ICEMAN projects, funded by Laboratory Directed Research and Development program and Compute and Data Environment for Science (CADES) at ORNL. The authors thank Dr. Dmitry Smirnov and Zhengguang Lu for assistance.

References

1. Sessoli, R.; Tsai, H. L.; Schake, A. R.; Wang, S.; Vincent, J. B.; Folting, K.; Gatteschi, D.; Christou, G.; Hendrickson, D. N., High-spin molecules: [$Mn_{12}O_{12}(O_2CR)_{16}(H_2O)_4$]. *J. Am. Chem. Soc.* **1993,** *115*, 1804-1816.

2. Sessoli, R.; Gatteschi, D.; Caneschi, A.; Novak, M. A., Magnetic bistability in a metal-ion cluster. *Nature* **1993,** *365*, 141-143.

3. Gatteschi, D.; Sessoli, R., Quantum Tunneling of Magnetization and Related Phenomena in Molecular Materials. *Angew. Chem. Int. Ed.* **2003,** *42*, 268-297.

4. Ishikawa, N.; Sugita, M.; Ishikawa, T.; Koshihara, S.-y.; Kaizu, Y., Lanthanide Double-Decker Complexes Functioning as Magnets at the Single-Molecular Level. *J. Am. Chem. Soc.* **2003,** *125*, 8694-8695.

5. Rinehart, J. D.; Long, J. R., Exploiting Single-Ion Anisotropy in the Design of *f*-Element Single-Molecule Magnets. *Chem. Sci.* **2011,** *2*, 2078-2085.

6. Woodruff, D. N.; Winpenny, R. E. P.; Layfield, R. A., Lanthanide Single-Molecule Magnets. *Chem. Rev.* **2013,** *113*, 5110-5148.

7. Liddle, S. T.; van Slageren, J., Improving f-Element Single Molecule Magnets. *Chem. Soc. Rev.* **2015,** *44*, 6655-6669.

8. Zhang, P.; Zhang, L.; Tang, J., Lanthanide single molecule magnets: Progress and perspective. *Dalton Trans.* **2015,** *44*, 3923-3929.

9. Lu, J.; Guo, M.; Tang, J., Recent Developments in Lanthanide Single-Molecule Magnets. *Chem. Asian J.* **2017,** *12*, 2772-2779.

10. Liu, J.-L.; Chen, Y.-C.; Tong, M.-L., Symmetry Strategies for High Performance Lanthanide-Based Single-Molecule Magnets. *Chem. Soc. Rev.* **2018,** *47*, 2431-2453.

11. Feng, M.; Tong, M.-L., Single Ion Magnets from 3d to 5f: Developments and Strategies. *Chem. Eur. J.* **2018,** *24*, 7574-7594.

12. Craig, G. A.; Murrie, M., 3d single-ion magnets. *Chem. Soc. Rev.* **2015,** *44*, 2135-2147.

13. Frost, J. M.; Harriman, K. L. M.; Murugesu, M., The rise of 3-d single-ion magnets in molecular magnetism: towards materials from molecules? *Chem. Sci.* **2016,** *7*, 2470-2491.

14. Gao, S., Ed., *Molecular Nanomagnets and Related Phenomena*. Springer: 2015.

15. Feltham, H. L. C.; Brooker, S., Review of Purely 4f and Mixed-Metal nd-4f Single-Molecule Magnets Containing only One Lanthanide Ion. *Coord. Chem. Rev.* **2014,** *276*, 1-33.

16. Layfield, R. A., Organometallic Single-Molecule Magnets. *Organometallics* **2014,** *33*, 1084-1099.

17. Jiang, S.-D.; Wang, B.-W.; Sun, H.-L.; Wang, Z.-M.; Gao, S., An Organometallic Single-Ion Magnet. *J. Am. Chem. Soc.* **2011,** *133*, 4730-4733.

18. Meihaus, K. R.; Long, J. R., Magnetic Blocking at 10 K and a Dipolar-Mediated Avalanche in Salts of the Bis(η^8-cyclooctatetraenide) Complex $[Er(COT)_2]^-$. *J. Am. Chem. Soc.* **2013,** *135*, 17952-17957.

19. Le Roy, J. J.; Korobkov, I.; Murugesu, M., A Sandwich Complex with Axial Symmetry for Harnessing the Anisotropy in a Prolate Erbium(III) Ion. *Chem. Comm.* **2014,** *50*, 1602-1604.

20. Palacios, M. A.; Titos-Padilla, S.; Ruiz, J.; Herrera, J. M.; Pope, S. J. A.; Brechin, E. K.; Colacio, E., Bifunctional $Zn^{II}Ln^{III}$ Dinuclear Complexes Combining Field Induced SMM Behavior and Luminescence: Enhanced NIR Lanthanide Emission by 9-Anthracene Carboxylate Bridging Ligands. *Inorg. Chem.* **2014,** *53*, 1465-1474.

21. Zhang, P.; Zhang, L.; Wang, C.; Xue, S.; Lin, S.-Y.; Tang, J., Equatorially Coordinated Lanthanide Single Ion Magnets. *J. Am. Chem. Soc.* **2014,** *136*, 4484-4487.

22. Chen, Y.-C.; Liu, J.-L.; Ungur, L.; Liu, J.; Li, Q.-W.; Wang, L.-F.; Ni, Z.-P.; Chibotaru, L. F.; Chen, X.-M.; Tong, M.-L., Symmetry-Supported Magnetic Blocking at 20 K in Pentagonal Bipyramidal Dy(III) Single-Ion Magnets. *J. Am. Chem. Soc.* **2016,** *138*, 2829-2837.

23. Liu, J.; Chen, Y.-C.; Liu, J.-L.; Vieru, V.; Ungur, L.; Jia, J.-H.; Chibotaru, L. F.; Lan, Y.; Wernsdorfer, W.; Gao, S.; Chen, X.-M.; Tong, M.-L., A Stable Pentagonal Bipyramidal Dy(III) Single-Ion Magnet with a Record Magnetization Reversal Barrier over 1000 K. *J. Am. Chem. Soc.* **2016,** *138*, 5441-5450.

24. Chen, Y. C.; Liu, J. L.; Wernsdorfer, W.; Liu, D.; Chibotaru, L. F.; Chen, X. M.; Tong, M. L., Hyperfine-Interaction-Driven Suppression of Quantum Tunneling at Zero Field in a Holmium(III) Single-Ion Magnet. *Angew. Chem. Int. Ed.* **2017,** *56*, 4996-5000.

25. Goodwin, C. A. P.; Ortu, F.; Reta, D.; Chilton, N. F.; Mills, D. P., Molecular Magnetic Hysteresis at 60 Kelvin in Dysprosocenium. *Nature* **2017,** *548*, 439.

26. Guo, F. S.; Day, B. M.; Chen, Y. C.; Tong, M. L.; Mansikkamäki, A.; Layfield, R. A., A Dysprosium Metallocene Single-Molecule Magnet Functioning at the Axial Limit. *Angew. Chem. Int. Ed.* **2017,** *56*, 11445-11449.

27. Bradley, D. C.; Ghotra, J. S.; Hart, F. A., Three-co-ordination in lanthanide chemistry: tris[bis(trimethylsilyl)amido]lanthanide(III) compounds. *J. Chem. Soc., Chem. Commun.* **1972**, 349-350.

28. Herrmann, W. A.; Anwander, R.; Munck, F. C.; Scherer, W.; Dufaud, V.; Huber, N. W.; Artus, G. R. J., Reaktivitätsbestimmender Einfluß der Ligandenkonstitution bei Seltenerdamiden: Herstellung und Struktur sterisch überladener Alkoxid-Komplexe. *Z. Naturforsch.* **1994,** *49b*, 1789-1797.

29. Zhang, P.; Jung, J.; Zhang, L.; Tang, J.; Le Guennic, B., Elucidating the Magnetic Anisotropy and Relaxation Dynamics of Low-Coordinate Lanthanide Compounds. *Inorg. Chem.* **2016,** *55*, 1905-1911.

30. Jank, S.; Amberger, H. D.; Edelstein, N. M., Electronic Structures of Highly-Symmetrical Compounds of f Elements: Part 30. Simulation of the Crystal Field Splitting Pattern of Tris(bis(trimethylsilyl)amido)erbium (III). *Spectrochim. Acta A* **1998,** *54*, 1645-1650.

31. AlDamen, M. A.; Clemente-Juan, J. M.; Coronado, E.; Martí-Gastaldo, C.; Gaita-Ariño, A., Mononuclear Lanthanide Single-Molecule Magnets Based on Polyoxometalates. *J. Am. Chem. Soc.* **2008,** *130*, 8874-8875.

32. Hallmen, P. P.; Köppl, C.; Rauhut, G.; Stoll, H.; van Slageren, J., Fast and reliable *ab initio* calculation of crystal field splittings in lanthanide complexes. *J. Chem. Phys.* **2017,** *147*, 164101.

33. Hallmen, P. P.; Rauhut, G.; Stoll, H.; Mitrushchenkov, A. O.; van Slageren, J., Crystal Field Splittings in Lanthanide Complexes: Inclusion of Correlation Effects beyond Second Order Perturbation Theory. *J. Chem. Theory Comput.* **2018,** *14*, 3998-4009.

34. Singh, S. K.; Gupta, T.; Shanmugam, M.; Rajaraman, G., Unprecedented Magnetic Relaxation via the Fourth Excited State in Low-Coordinate Lanthanide Single-Ion Magnets: A Theoretical Perspective. *Chem. Commun.* **2014,** *50*, 15513-15516.

35. Hill, J. C.; Wheeler, R. G., Far-Infrared Spectra of Erbium, Dysprosium, and Samarium Ethyl Sulphate. *Phys. Rev.* **1966,** *152*, 482-494.

36. Bloor, D.; Copland, G. M., Far Infrared Spectra of Magnetic Ions in Crystals. *Rep. Prog. Phys.* **1972,** *35*, 1173.

37. Sievers, A. J.; Tinkham, M., Far Infrared Spectra of Rare-Earth Iron Garnets. *Phys. Rev.* **1963,** *129*, 1995-2004.

38. Hadni, A.; Morlot, G.; Strimer, P., Far-Infrared Electronic Transitions in Solids. *IEEE J. Quantum Electron.* **1967,** *3*, 111-116.

39. Slota, M.; Jiang, S.-D.; Heintze, E.; Rechkemmer, Y.; Dressel, M.; van Slageren, J.; Bogani, L., Accurate and Unequivocal Determination of the Crystal-Field Parameters of Lanthanide Ions via a Multitechnique Approach. *Phys. Rev. B* **2019,** *99*, 134410.

40. Perfetti, M.; Gysler, M.; Rechkemmer-Patalen, Y.; Zhang, P.; Taştan, H.; Fischer, F.; Netz, J.; Frey, W.; Zimmermann, L. W.; Schleid, T.; Hakl, M.; Orlita, M.; Ungur, L.; Chibotaru, L.; Brock-Nannestad, T.; Piligkos, S.; van Slageren, J., Determination of the Electronic Structure of a Dinuclear Dysprosium Single Molecule Magnet without Symmetry Idealization. *Chem. Sci.* **2019,** *10*, 2101-2110.

41. Rechkemmer, Y.; Fischer, J. E.; Marx, R.; Dörfel, M.; Neugebauer, P.; Horvath, S.; Gysler, M.; Brock-Nannestad, T.; Frey, W.; Reid, M. F.; van Slageren, J., Comprehensive Spectroscopic Determination of the Crystal Field Splitting in an Erbium Single-Ion Magnet. *J. Am. Chem. Soc.* **2015,** *137*, 13114-13120.

42. Marx, R.; Moro, F.; Dorfel, M.; Ungur, L.; Waters, M.; Jiang, S. D.; Orlita, M.; Taylor, J.; Frey, W.; Chibotaru, L. F.; van Slageren, J., Spectroscopic Determination of Crystal Field Splittings in Lanthanide Double Deckers. *Chem. Sci.* **2014,** *5*, 3287-3293.

43. Zvyagin, S. A.; Ozerov, M.; Čižmár, E.; Kamenskyi, D.; Zherlitsyn, S.; Herrmannsdörfer, T.; Wosnitza, J.; Wünsch, R.; Seidel, W., Terahertz-Range Free-Electron Laser Electron Spin Resonance Spectroscopy: Techniques and Applications in High Magnetic Fields. *Rev. Sci. Instrum* **2009,** *80*, 073102.

44. Ozerov, M.; Bernáth, B.; Kamenskyi, D.; Redlich, B.; van der Meer, A. F. G.; Christianen, P. C. M.; Engelkamp, H.; Maan, J. C., A THz Spectrometer Combining the Free Electron Laser FLARE with 33 T Magnetic Fields. *Appl. Phys. Lett.* **2017,** *110*, 094106.

45. Cotton, F. A., *Chemical Applications of Group Theory*. 3 ed.; Wiley: New York, 1971.

46. Pedersen, K. S.; Ungur, L.; Sigrist, M.; Sundt, A.; Schau-Magnussen, M.; Vieru, V.; Mutka, H.; Rols, S.; Weihe, H.; Waldmann, O.; Chibotaru, L. F.; Bendix, J.; Dreiser, J., Modifying the Properties of 4f Single-Ion Magnets by Peripheral Ligand Functionalisation. *Chem. Sci.* **2014,** *5*, 1650-1660.

47. Pedersen, K. S.; Dreiser, J.; Weihe, H.; Sibille, R.; Johannesen, H. V.; Sørensen, M. A.; Nielsen, B. E.; Sigrist, M.; Mutka, H.; Rols, S.; Bendix, J.; Piligkos, S., Design of Single-Molecule Magnets: Insufficiency of the Anisotropy Barrier as the Sole Criterion. *Inorg. Chem.* **2015,** *54*, 7600-7606.

48. Urland, W.; Kremer, R.; Furrer, A., Crystal Field Levels in Tetraphenylarsoniumpentakis(nitrato)ytterbate(III) Determined by Neutron Spectroscopy. *Chem. Phys. Lett.* **1986,** *132*, 113-115.

49. Baker, M. L.; Tanaka, T.; Murakami, R.; Ohira-Kawamura, S.; Nakajima, K.; Ishida, T.; Nojiri, H., Relationship between Torsion and Anisotropic Exchange Coupling in a Tb^{III}-Radical-Based Single-Molecule Magnet. *Inorg. Chem.* **2015,** *54*, 5732-5738.

50. Dunstan, M. A.; Mole, R. A.; Boskovic, C., Inelastic Neutron Scattering of Lanthanoid Complexes and Single-Molecule Magnets. *Eur. J. Inorg. Chem.* **2019**, 1090-1105.

51. Xue, Z.-L.; Ramirez-Cuesta, A. J.; Brown, C. M.; Calder, S.; Cao, H.; Chakoumakos, B. C.; Daemen, L. L.; Huq, A.; Kolesnikov, A. I.; Mamontov, E.; Podlesnyak, A. A.; Wang,

X., Neutron Instruments for Research in Coordination Chemistry. *Eur. J. Inorg. Chem.* **2019**, 1065-1089.

52. Bacon, G. E., *Neutron Scattering in Chemistry*. Butterworth: London, 1977.
53. Stavretis, S. E.; Atanasov, M.; Podlesnyak, A. A.; Hunter, S. C.; Neese, F.; Xue, Z.-L., Magnetic transitions in iron porphyrin halides by inelastic neutron scattering and *ab initio* studies of zero-field splittings. *Inorg. Chem.* **2015,** *54*, 9790-9801.
54. Hunter, S. C.; Podlesnyak, A. A.; Xue, Z.-L., Magnetic excitations in metalloporphyrins by Inelastic Neutron Scattering: Determination of zero-field splittings in iron, manganese, and chromium complexes. *Inorg. Chem.* **2014,** *53*, 1955-1961.
55. Furrer, A.; Mesot, J.; Strässle, T., *Neutron Scattering in Condensed Matter Physics*. World Scientific: 2009.
56. Dobe, C.; Strässle, T.; Juranyi, F.; Tregenna-Piggott, P. L. W., Pressure-Induced Switch of the Direction of the Unique Jahn−Teller Axis of the Chromium(II) Hexaqua Cation in the Deuterated Ammonium Chromium Tutton Salt. *Inorg. Chem.* **2006,** *45*, 5066-5072.
57. Moseley, D. H.; Stavretis, S. E.; Thirunavukkuarasu, K.; Ozerov, M.; Cheng, Y.; Daemen, L. L.; Ludwig, J.; Lu, Z.; Smirnov, D.; Brown, C. M.; Pandey, A.; Ramirez-Cuesta, A. J.; Lamb, A. C.; Atanasov, M.; Bill, E.; Neese, F.; Xue, Z.-L., Spin–Phonon Couplings in Transition Metal Complexes with Slow Magnetic Relaxation. *Nat. Commun.* **2018,** *9*, 2572.
58. Mitchell, P. C. H.; Parker, S. F.; Ramirez-Cuesta, A. J.; Tomkinson, J., *Vibrational Spectroscopy with Neutrons: With Applications in Chemistry, Biology, Materials Science and Catalysis*. World Scientific Publishing Company: 2005; Vol. 3.

59. Hudson, B. S., Vibrational Spectroscopy via Inelastic Neutron Scattering. In *Frontiers of Molecular Spectroscopy*, Laane, J., Ed. Elsevier: Amsterdam, 2009; pp 597-622.

60. Mitchell, P. C. H.; Parker, S. F.; Ramirez-Cuesta, A. J.; Tomkinson, J., *Vibrational Spectroscopy with Neutrons: With Applications in Chemistry, Biology, Materials Science and Catalysis*. World Scientific Publishing Company: 2005.

61. Dove, M. T., *Introduction to Lattice Dynamics*. Cambridge University Press: 1993; Vol. Cambridge Topics in Mineral Physics and Chemistry

62. Benelli, C.; Gatteschi, D., Single Ion Magnet (SIM). In *Introduction to Molecular Magnetism*, Wiley-VCH: 2015; pp 217-237.

63. Krzystek, J.; Telser, J., Measuring giant anisotropy in paramagnetic transition metal complexes with relevance to single-ion magnetism. *Dalton Trans.* **2016,** *45*, 16751-16763.

64. McInnes, E. J. L.; Winpenny, R. E. P., Molecular Magnets. In *Comprehensive Inorganic Chemistry II*, Poeppelmeier, K., Ed. Elsevier: Amsterdam, 2013; pp 371-395.

65. Neese, F.; Pantazis, D. A., What is not required to make a single molecule magnet. *Faraday Discuss.* **2011,** *148*, 229-238.

66. Demir, S.; Jeon, I.-R.; Long, J. R.; Harris, T. D., Radical ligand-containing single-molecule magnets. *Coord. Chem. Rev.* **2015,** *289*, 149-176.

67. Orbach, R.; Stapleton, H. J., Electron Spin-Lattice Relaxation. In *Electron Paramagnetic Resonance*, Geschwind, S., Ed. Plenum Press: New York, 1972; pp 121-216.

68. Lunghi, A.; Totti, F.; Sanvito, S.; Sessoli, R., Intra-Molecular Origin of the Spin-Phonon Coupling in Slow-Relaxing Molecular Magnets. *Chem. Sci.* **2017,** *8*, 6051-6059.

69. Escalera-Moreno, L.; Suaud, N.; Gaita-Ariño, A.; Coronado, E., Determining Key Local Vibrations in the Relaxation of Molecular Spin Qubits and Single-Molecule Magnets. *J. Phys. Chem. Lett.* **2017,** *8*, 1695-1700.

70. Hizhnyakov, V.; Pae, K.; Vaikjärv, T., Optical Jahn–Teller effect in the case of local modes and phonons. *Chem. Phys. Lett.* **2012,** *525-526*, 64-68.

71. Pae, K.; Hizhnyakov, V., Nonadiabaticity in a Jahn-Teller system probed by absorption and resonance Raman scattering. *J. Chem. Phys.* **2013,** *138*, 104103.

72. Palii, A.; Ostrovsky, S.; Reu, O.; Tsukerblat, B.; Decurtins, S.; Liu, S.-X.; Klokishner, S., Microscopic theory of cooperative spin crossover: Interaction of molecular modes with phonons. *J. Chem. Phys.* **2015,** *143*, 084502.

73. Palii, A.; Ostrovsky, S.; Reu, O.; Tsukerblat, B.; Decurtins, S.; Liu, S.-X.; Klokishner, S., Diversity of Spin Crossover Transitions in Binuclear Compounds: Simulation by Microscopic Vibronic Approach. *J. Phys. Chem. C* **2016,** *120*, 14444-14453.

74. Rechkemmer, Y.; Breitgoff, F. D.; van der Meer, M.; Atanasov, M.; Hakl, M.; Orlita, M.; Neugebauer, P.; Neese, F.; Sarkar, B.; van Slageren, J., A Four-Coordinate Cobalt(II) Single-Ion Magnet with Coercivity and a Very High Energy Barrier. *Nat. Commun.* **2016,** *7*, 10467.

75. Stavretis, S. E.; Cheng, Y.; Daemen, L. L.; Brown, C. M.; Moseley, D. H.; Bill, E.; Atanasov, M.; Ramirez-Cuesta, A. J.; Neese, F.; Xue, Z.-L., Probing Magnetic Excitations in Co^{II} Single-Molecule Magnets by Inelastic Neutron Scattering. *Eur. J. Inorg. Chem.* **2019**, 1119-1127.

76. Stavretis, S. E.; Mamontov, E.; Moseley, D. H.; Cheng, Y.; Daemen, L. L.; Ramirez-Cuesta, A. J.; Xue, Z.-L., Effect of magnetic fields on the methyl rotation in a

paramagnetic cobalt(II) complex. Quasielastic neutron scattering studies. *Phys. Chem. Chem. Phys.* **2018,** *20*, 21119-21126.

77. Stavretis, S. E.; Moseley, D. H.; Fei, F.; Cui, H.-H.; Cheng, Y.; Podlesnyak, A. A.; Wang, X.; Daemen, L. L.; Hoffmann, C. M.; Ozerov, M.; Lu, Z.; Thirunavukkuarasu, K.; Smirnov, D.; Chang, T.; Chen, Y.-S.; Ramirez-Cuesta, A. J.; Chen, X.-T.; Xue, Z.-L., Spectroscopic Studies of the Magnetic Excitation and Spin-Phonon Couplings in a Single-Molecule Magnet. *Chem. Eur. J.* **2019,** *25*, 15846–15857.
78. DCS website: https://ncnr.nist.gov/instruments/dcs/.
79. VISION website: https://neutrons.ornl.gov/vision.
80. Görller-Walrand, C.; Binnemans, K., Handbook on the Physics and Chemistry of Rare Earths. Gschneider, K. A.; Eyring, L., Eds. Elsevier: Amsterdam, 1998; Vol. 25, pp 101-264.
81. Rogers, P. D.; Choi, Y. J.; Standard, E. C.; Kang, T. D.; Ahn, K. H.; Dubroka, A.; Marsik, P.; Wang, C.; Bernhard, C.; Park, S.; Cheong, S. W.; Kotelyanskii, M.; Sirenko, A. A., Adjusted oscillator strength matching for hybrid magnetic and electric excitations in $Dy_3Fe_5O_{12}$ garnet. *Phys. Rev. B* **2011,** *83*, 174407.
82. Sirenko, A. A.; O'Malley, S. M.; Ahn, K. H.; Park, S.; Carr, G. L.; Cheong, S. W., Infrared-active excitations related to Ho^{3+} ligand-field splitting at the commensurate-incommensurate magnetic phase transition in $HoMn_2O_5$. *Phys. Rev. B* **2008,** *78*, 174405.
83. Koster, G. F.; Dimmock, J. O.; Wheeler, R. G.; Statz, H., *Properties of the Thirty-Two Point Groups*. MIT Press: 1963; p 51.
84. Jacobs, P. W. M., *Group Theory with Applications in Chemical Physics*. Cambridge University Press: 2005; p 447.

85. Cohen-Tannoudji, C.; Laloë, F.; Diu, B., *Quantum Mechanics*. Wiley: New York, 1977; Vol. 1.

86. Frank, W.; von Brentano, P., Classical Analogy to Quantum Mechanical Level Repulsion. *Am. J. Phys.* **1994,** *62*, 706-709.

87. Copley, J. R. D.; Cook, J. C., The Disk Chopper Spectrometer at NIST: A New Instrument for Quasielastic Neutron Scattering Studies. *Chem. Phys.* **2003,** *292*, 477-485.

88. Seeger, P. A.; Daemen, L. L.; Larese, J. Z., Resolution of VISION, A Crystal-Analyzer Spectrometer. *Nucl. Instr. Meth. Phys. Res. A* **2009,** *604*, 719-728.

89. Carpenter, J. M.; Loong, C. K., *Elements of Slow-Neutron Scattering: Basics, Techniques, and Applications*. Cambridge University Press: Cambridge, 2015.

90. Mitchell, P. C. H.; Parker, S. F.; Ramirez-Cuesta, A. J.; Tomkinson, J., *Vibrational Spectroscopy with Neutrons: With Applications in Chemistry, Biology, Materials Science and Catalysis*. World Scientific Publishing Company: 2005.

91. Kresse, G.; Furthmüller, J., Efficient Iterative Schemes for Ab initio Total-Energy Calculations using a Plane-Wave Basis Set. *Phys. Rev. B* **1996,** *54*, 11169-11186.

92. Henkelman, G.; Uberuaga, B. P.; Jónsson, H., A climbing image nudged elastic band method for finding saddle points and minimum energy paths. *J. Chem. Phys.* **2000,** *113*, 9901-9904.

93. Infrared/Terahertz Magneto Optics in DC Fields website: https://nationalmaglab.org/user-facilities/dc-field/dcfield-techniques/magneto-optics-ir-thz-dc.

94. Clark, R. J. H.; Dines, T. J., Electronic Raman Spectroscopy. In *Advances in Infrared and Raman Spectroscopy*, Clark, R. J. H.; Hester, R. E., Eds. Heyden & Son: London, 1982; Vol. 9, pp 282-360.

95. Long, D. A., *The Raman Effect. A Unified Treatment of the Theory of Raman Scattering by Molecules (Ch. 9, pp. 289-302 for Electronic Raman)*. 1st ed.; Wiley: 2001.

96. Kiel, A.; Porto, S. P. S., Selection rules for the electronic Raman effect. *J. Mol. Spectrosc.* **1969,** *32*, 458-468.

97. Azuah, R. T.; Kneller, L. R.; Qiu, Y.; Tregenna-Piggott, P. L. W.; Brown, C. M.; Copley, J. R. D.; Dimeo, R. M., DAVE: A Comprehensive Software Suite for the Reduction, Visualization, and Analysis of Low Energy Neutron Spectroscopic Data. *J. Res. Nat. Inst. Stand. Technol.* **2009,** *114*, 341-358.

98. For space Group 163 : *P*-31*c*, see, e.g., http://img.chem.ucl.ac.uk/sgp/large/163a.htm.

99. Kresse, G.; Joubert, D., From Ultrasoft Pseudopotentials to the Projector Augmented-Wave Method. *Phys. Rev. B* **1999,** *59*, 1758-1775.

100. Blöchl, P. E., Projector Augmented-Wave Method. *Phys. Rev. B* **1994,** *50*, 17953-17979.

101. Perdew, J. P.; Burke, K.; Ernzerhof, M., Generalized Gradient Approximation Made Simple. *Phys. Rev. Lett.* **1996,** *77*, 3865-3868.

102. Fu, Y.; Huang, Z.; Wang, X.; Ye, L., The Strong Correlation of the 4f Electrons of Erbium in Silicon. *J. Phys. Condens. Matter* **2003,** *15*, 1437-1444.

103. Deilynazar, N.; Khorasani, E.; Alaei, M.; Javad Hashemifar, S., First-Principles Insights into f Magnetism: A Case Study on some Magnetic Pyrochlores. *J. Magn. Magn. Mater.* **2015,** *393*, 127-131.

104. Klimeš, J.; Bowler, D. R.; Michaelides, A., Chemical Accuracy for the Van der Waals Density Functional. *J. Phys. Condens. Matter* **2010,** *22*, 022201.

105. Togo, A.; Tanaka, I., First Principles Phonon Calculations in Materials Science. *Scr. Mater.* **2015,** *108*, 1-5.

106. Phonopy website: https://atztogo.github.io/phonopy/index.html.

For Table of Contents Only

Magnetic transitions in single-molecule magnet (SMM) $Er[N(SiMe_3)_2]_3$ have been determined by far-IR and inelastic neutron scattering (INS) under applied magnetic fields. Spin–phonon couplings between IR-active phonons and Kramers doublets in such a lanthanide molecular complex are observed for the first time with coupling constants ≈ 2-3 cm^{-1}. INS also gives complete phonon spectra of the complex. Periodic DFT computations provide the energies of all phonon excitations, which compare well with the INS spectra.